WILEY

# Data-driven variational multiscale reduced order modeling of vaginal tissue inflation

William Snyder[1] | Jeffrey A. McGuire[1] | Changhong Mou[2] | David A. Dillard[3] | Traian Iliescu[2] | Raffaella De Vita[1]

[1]STRETCH Lab, Department of Biomedical Engineering and Mechanics, Virginia Tech, Blacksburg, Virginia, USA

[2]Department of Mathematics, Virginia Tech, Blacksburg, Virginia, USA

[3]Department of Biomedical Engineering and Mechanics, Virginia Tech, Blacksburg, Virginia, USA

**Correspondence**
Raffaella De Vita, STRETCH Lab, Department of Biomedical Engineering and Mechanics, Virginia Tech, 335 Kelly Hall, 325 Stanger Street, Blacksburg, VA 24061, USA.
Email: devita@vt.edu

## Abstract

The vagina undergoes large finite deformations and has complex geometry and microstructure, resulting in material and geometric nonlinearities, complicated boundary conditions, and nonhomogeneities within finite element (FE) simulations. These nonlinearities pose a significant challenge for numerical solvers, increasing the computational time by several orders of magnitude. Simplifying assumptions can reduce the computational time significantly, but this usually comes at the expense of simulation accuracy. This study proposed the use of reduced order modeling (ROM) techniques to capture experimentally measured displacement fields of rat vaginal tissue during inflation testing in order to attain both the accuracy of higher-fidelity models and the speed of simpler simulations. The proper orthogonal decomposition (POD) method was used to extract the significant information from FE simulations generated by varying the luminal pressure and the parameters that introduce the anisotropy in the selected constitutive model. A new data-driven (DD) variational multiscale (VMS) ROM framework was extended to obtain the displacement fields of rat vaginal tissue under pressure. For comparison purposes, we also investigated the classical Galerkin ROM (G-ROM). In our numerical study, both the G-ROM and the DD-VMS-ROM decreased the FE computational cost by orders of magnitude without a significant decrease in numerical accuracy. Furthermore, the DD-VMS-ROM improved the G-ROM accuracy at a modest computational overhead. Our numerical investigation showed that ROM has the potential to provide efficient and accurate computational tools to describe vaginal deformations, with the ultimate goal of improving maternal health.

**KEYWORDS**
data-driven modeling, reduced order modeling, vaginal tissue

# 1 | INTRODUCTION

The rate of cesarean sections has increased globally, with latest available data from 154 countries showing that cesarean sections account for 21.1% of births.[1] In the U.S., the overall rate of cesarean sections was 31.7% in 2019 and the rate of low-risk cesarean sections was 25.6% in the same year.[2] Many factors have contributed to the rise of these rates, such as public perception that the cesarean delivery is safer than vaginal delivery by preventing pelvic organ trauma and the widespread practice of defensive medicine among obstetricians. Compared to vaginal delivery, cesarean delivery is associated with increased maternal mortality and morbidity such as postpartum hemorrhage, hysterectomy, and uterine infections.[3] To reduce the number of unnecessary cesarean sections and improve maternal health outcomes, new scientific-based methods that predict the potential trauma from delivery in real-time are needed so that the safest mode of delivery can be selected by obstetricians.

In vivo testing methodologies to characterize the properties of reproductive tissues and guide the selection of the mode of delivery may be invasive, endangering the mothers and their babies. Alternatively, in silico methods that describe the behavior of the reproductive system during pregnancy and childbirth are ideal since they can potentially predict non-invasively the clinical outcome of labor. An extensive review of childbirth computational models has been recently published.[4] Several studies have developed subject-specific finite element (FE) models that use MRI scans of volunteers to construct the geometry of pelvic floor organs, demonstrating the potential for customization of childbirth models to individual patients.[5–7] Unfortunately, due to the complex geometries, boundary conditions, nonlinear constitutive models, and large deformations of the reproductive system, sophisticated FE full order models (FOMs) are computationally expensive. Thus, they remain impractical as real-time predictive tools for patient-specific interventions. One approach to address these limitations is to create reduced order models (ROMs) of the reproductive system.

The goal of developing ROMs is to reduce the FOMs' computational cost by orders of magnitude without significantly reducing their numerical accuracy. Various approaches may be used to accomplish this aim, and some of the most popular are projection-based ROM methods, such as the proper orthogonal decomposition (POD),[8,9] reduced basis method,[10,11] proper generalized decomposition,[12] and hierarchical model reduction.[13,14] Using projection-based ROMs, the space of the FOM with a large number of degrees of freedom (e.g., $O[10^6]$) is projected onto a subspace with far fewer degrees of freedom (e.g., $O[10^1]$). POD is one of the most common approaches for projection-based ROM in the fields of fluid and solid mechanics. While the reduced subspace significantly decreases the size of the system of equations to be solved, computation of nonlinearities is still required at the FOM space, thus limiting the POD-ROM effectiveness. To reduce this computational overhead, different hyper-reduction approaches have been proposed, for example, the empirical interpolation method[15] and the discrete empirical interpolation method.[16]

ROM techniques have been proposed for real-time simulations of soft tissue deformations for surgical planning and minimally invasive surgery. Complex simulations of the heart with isotropic, anisotropic, viscoelastic, and active material models have successfully been approximated by reduced basis approaches.[17–20] Some relevant work using proper generalized decomposition on cardiac conductivities has also been published.[21] Other tissues modeled by ROM include the liver,[22–25] cornea,[23,25–27] and inferior turbinate.[28,29] Several of the cited investigators have explored various projection-based model reduction methods,[30] discrete empirical interpolation methods,[30] and hyper-reduction enhancements[18,19,25,30] to handle nonlinearities that characterize soft tissue simulations. However, to our knowledge, model reduction techniques such as POD have not been used to simulate the real-time deformations of the highly nonlinear and anisotropic tissues of the reproductive system, especially the very large deformations during childbirth.

In this work, we propose reduced order modeling as an efficient and accurate means of approximating the vaginal tissue deformation. To this end, we first use our knowledge of the ex vivo micro-structural and mechanical behavior of the rat vaginal tissue from experimental data[31,32] to develop a FOM using the FE method. We then investigate the feasibility of ROM techniques to approximate the deformations of the rat vagina subjected to various levels of luminal pressure and having different collagen fiber organization. More specifically, we extend a newly developed data-driven (DD) ROM framework to a soft tissue mechanics problem, and we compare it with a classical projection-based ROM approach both in terms of accuracy and computational cost. This work is a proof-of-concept that demonstrates the potential of ROM techniques for the development of real-time predictive tools for maternal health.

# 2 | FULL ORDER MODEL

In this section, we present the first FE model that describes the boundary and loading conditions of rat vaginal tissue during inflation experiments. By changing the orientation of collagen fibers in the constitutive model selected for

vaginal tissue, as well as the applied luminal pressure, we generate a set of FOM solutions. This set of solutions constitute the snapshots that are then used to create the ROM solutions as described in Section 3.

## 2.1 | Mathematical model and physical parameters

The geometry, boundary conditions, and material parameters used to construct the FE model that describes the deformations of rat vaginal specimens subjected to luminal pressure were selected to approximate experimental data.[31,32] During the experiments, the vaginal tissue was mounted onto dispensing needles and inflated via a pressure pump with phosphate buffered saline. One dispensing needle was fixed while the other dispensing needle could slide freely along the axial direction of the rat vaginal specimens to allow deformations in both axial and hoop directions. The tissue was pre-loaded to an internal pressure of 1.4 kPa prior to collecting the experimental data. Thus, we constructed our model geometry based on the shape and average dimensions of the vaginal tissue specimens with the applied pre-load, as well as the outer diameters of the dispensing needles.[31] Construction of the model and subsequent finite simulations for the vaginal tissue were carried out within Abaqus/Standard (Abaqus 2020, Dassault Systèmes Americas Corp., Waltham, MA). All simulations were performed on a 24-core Intel® Xeon® Gold 6248R CPU @ 3.00GHz with 191 GB of usable RAM.

Figure 1A displays the assumed geometry of the pressurized vaginal specimen with dimensions and relevant anatomical regions of the vagina. The geometry resembled a hollow prolate spheroid with an initial maximum outer diameter at mid-span of 10.2 mm, a uniform thickness of .3 mm, and a height of 12 mm. With respect to the axial direction,
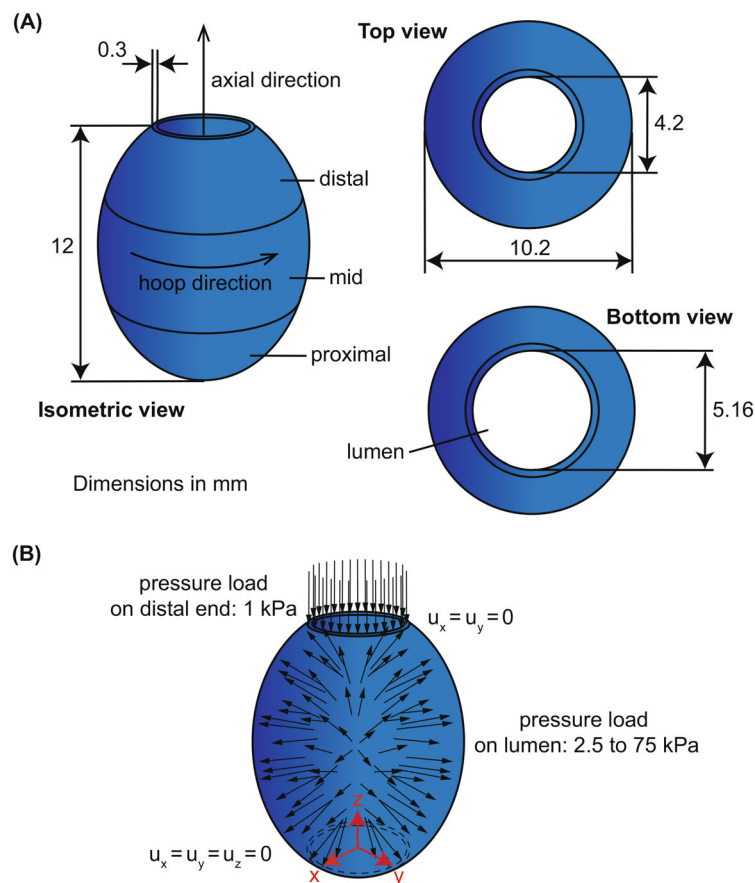


**FIGURE 1** (A) Isometric, top, and bottom views of the rat vaginal specimen with dimensions and anatomical (proximal, mid, and distal) regions. (B) Boundary conditions for the rat vaginal specimen used to simulate inflation testing. The annotations $u_x$, $u_y$, and $u_z$ denote the translational displacements of nodes at the boundaries, respectively. The uppermost distal surface was fixed in the hoop and radial directions and subjected to a constant pressure in the axial direction, while the lowermost proximal surface was fixed. The lumen was subjected to a surface pressure which was incremented through 30 quasi-static steps, $p_1 = 2.5$ kPa, $\cdots, p_{30} = 75$ kPa.

the top, middle, and bottom thirds of the model geometry corresponded to the distal, mid, and proximal anatomical regions of the vagina, respectively. The inner diameter of the opening at the distal end was set to 4.2 mm and the inner diameter of the opening at the proximal end was set to 5.16 mm.

Figure 1B displays the selected global Cartesian coordinate system with the base of the proximal end centered at the origin. This figure also lists the boundary conditions of the model. Following the experimental setup, the lowermost surface of the proximal end of the model was fixed. The uppermost surface of the distal end was fixed in the hoop and radial directions, but had no prescribed displacement in the axial direction. Uniform pressure boundary conditions were applied normal to the internal surface (lumen) and the uppermost distal surface. The pressure on the uppermost distal surface was included to account for the weight of the upper needle acting on the tissue. Pressures were applied in the model with ramp functions starting from 0 kPa. The maximum pressure on the uppermost distal surface was set to 1 kPa in all simulations to account for the upper needle. This value was chosen so that the simulation would reflect the behavior observed in experiments where no negative axial strain occurred using a pre-load of 1.4 kPa.[31] Abaqus outputs for displacement were recorded at the final step of each ramp function to create a quasi-static snapshot corresponding to a given pressure on the lumen.

To simulate the constitutive behavior of the vagina, the Holzapfel-Gasser-Ogden strain energy model was selected.[33] According to the model, the strain energy per unit reference volume of the tissue is given by

$$W = \frac{c}{2}(\overline{I}_1 - 3) + \frac{1}{D}\left[\frac{(J)^2 - 1}{2} - \ln J\right] + \frac{k_1}{2k_2}\sum_{\alpha=1}^{2}\left\{e^{[k_2\langle\overline{E}_\alpha\rangle^2]} - 1\right\}, \tag{1}$$

with

$$\overline{E}_\alpha = \kappa(\overline{I}_1 - 3) + (1 - 3\kappa)(\overline{I}_{4(\alpha\alpha)} - 1), \tag{2}$$

where $c$, $D$, $k_1$, $k_2$, and $\kappa$ are material parameters; $\overline{I}_1$ is the first deviatoric strain invariant of $\overline{C}$; $J$ is the elastic volume ratio given by the determinant, $J$, of the deformation gradient, $F$; and $\overline{I}_{4(\alpha\alpha)} = a_\alpha\overline{C}a_\alpha$ is a pseudo-invariant of $\overline{C}$ and $a_\alpha$ is a set of unit vectors that characterize the mean preferred direction of the fibers in the reference configuration. This form of the strain energy results from a deviatoric-dilational multiplicative split that is used for simplifying numerical implementation.[34] As such, $\overline{C} = J^{-2/3}C$, where $C = F^\top F$ is the right Cauchy-Green strain tensor. The operator $\langle \cdot \rangle$ in Equation (1) denotes the Macauley bracket.

This form of the Holzapfel-Gasser-Ogden model assumes that two families of fibers are dispersed about mean preferred directions, $a_1$ and $a_2$, with rotational symmetry and that all families of fibers possess the same mechanical properties, $k_1$ and $k_2$, and level of dispersion, $\kappa$, where $0 \leq \kappa \leq 1/3$. In Abaqus, the material coordinates which described $a_1$ and $a_2$ were defined via pseudo-cylindrical local Cartesian coordinate systems for each node. These local Cartesian coordinate directions were denoted as $x'$, $y'$, and $z'$. The $z'$-direction was always aligned with the $z$-direction from the global Cartesian coordinate system shown in Figure 1. The local radial direction, $x'$, was defined as aligned with the ray that was orthogonal to the global $z$-axis and extended from the global $z$-axis to the given node. The local tangential direction, $y'$, was defined as aligned with the ray orthogonal to both $x'$ and $z'$ that pointed in the direction of counter-clockwise rotation about the global $z$-axis. For this study, fibers were oriented in the hoop-axial plane of the vagina which was equivalent to the $x'$-$z'$ plane at each node. Thus, Abaqus' pseudo-cylindrical scheme described mean preferred fiber directions in the hoop-axial plane using local Cartesian coordinates for $a_1$ and $a_2$.

The mean preferred fiber directions, $a_1 = (0, \cos\beta, \sin\beta)$ and $a_2 = (0, \cos\beta, -\sin\beta)$, and fiber dispersion parameter, $\kappa$, were chosen to be representative of the collagen fiber organization that was measured experimentally in the tangential (or hoop-axial) plane of the vagina (Figure 9 in reference 32). The angle $\beta$ was defined relative to the hoop direction of the vagina, that is the hoop direction was at a 0° angle. The value of this angle in the distal, mid, and proximal regions of the vagina was defined as $\beta_d$, $\beta_m$, and $\beta_p$, respectively. Then, within each of the three anatomical regions of the vagina, both families of fibers had the same mean preferred fiber orientation relative to the hoop direction, but one family of fibers had positive orientation angles and the other negative orientation angles.

The model parameters in Equation (1) were selected to be $c = 6$ kPa, $D = .01$, $k_1 = 15$ kPa, $k_2 = 15$, and $\kappa = .25$. This selection was made by varying the parameters $c$, $D$, $k_1$, and $k_2$, starting from previous values reported in the literature,[33] so that the average of the pressure versus strain data computed over a subset of nodes in the mid region of the vagina

was comparable to reported experimental data (Figure 2). For this validation, the mean preferred fiber orientations were set to $\beta_d = \beta_m = 35°$ and $\beta_p = 55°$, and $k_2$ was always set to be numerically equivalent to $k_1$.

## 2.2 | Finite element method

For any given set of mean preferred fiber directions defined by $\mu_i$ reported in Table 1, FE solutions at 30 different luminal pressures, $p_1 = 2.5$ kPa, $p_2 = 5$ kPa, $p_3 = 7.5$ kPa, ..., $p_{30} = 75$ kPa, were obtained. The pressure was increased from 2.5 kPa to 75 kPa, in equal increments of 2.5 kPa. In Abaqus, an automatic scheme was selected for the pressure ramp function that increments the load condition from 0 kPa to the target pressure of a given simulation in steps defined as
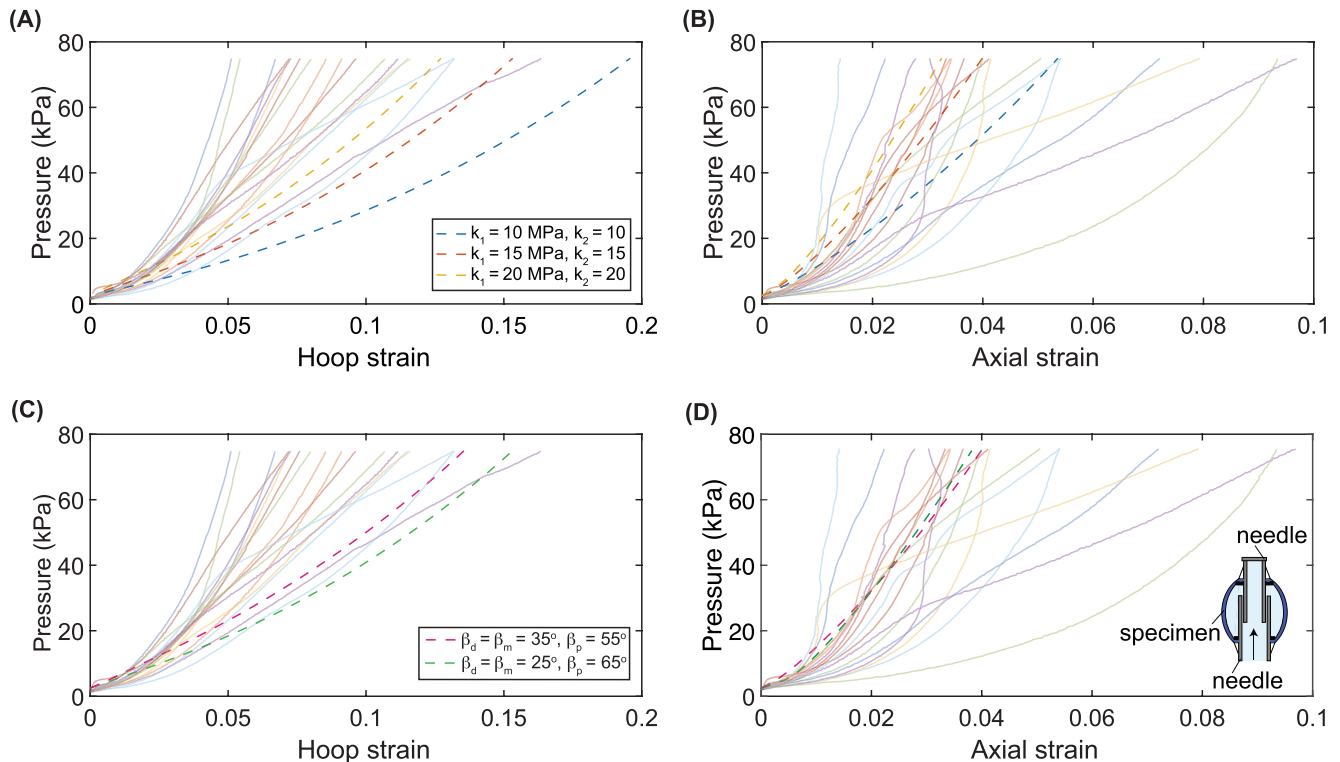


**FIGURE 2** Experimental pressure versus hoop strain and pressure versus axial strain data (continuous lines) with FE corresponding predictions (dashed lines) at (A), (B) various $k_1$ and $k_2$ and (C), (D) various $\beta_d$, $\beta_m$, and $\beta_p$. The insert in (d) is a schematic of the transverse cross-section of the coaxial needles holding a vaginal specimen.

**TABLE 1** Mean preferred fiber orientations for the distal, mid, and proximal regions of the vagina used to generate the snapshots for the ROMs. The orientations were defined relative to the hoop direction of the vagina

| Parameter set | $\beta_d$ | $\beta_m$ | $\beta_p$ |
| --- | --- | --- | --- |
| $\mu_1$ | 35° | 35° | 55° |
| $\mu_2$ | 35° | 35° | 65° |
| $\mu_3$ | 25° | 25° | 65° |
| $\mu_4$ | 35° | 25° | 55° |
| $\mu_5$ | 25° | 35° | 55° |
| $\mu_6$ | 35° | 25° | 65° |
| $\mu_7$ | 25° | 35° | 65° |
| $\mu_8$ | 25° | 25° | 55° |

fractions of the target pressure. The initial step size was set to $10^{-3}$ times the target pressure, and the minimum step size to $10^{-8}$ times the target pressure. The iterative Newton–Raphson solver was used to solve the resulting nonlinear system for each pressure value. When the solver failed to converge with the initial step size, it reduced the step size within the bounds until convergence was achieved and continued to the target pressure.

To determine the FOM (FE) solution for each set of parameters, $\mu_1, ..., \mu_8$, at each of the luminal pressure values, $p_1$, $p_2, p_3, ..., p_{30}$, a total of $n = 8 \times 30$ nonlinear systems of equations were solved in Abaqus using the Newton–Raphson method. The final Newton–Raphson iterations of the weak form of the equilibrium equations for each set of parameters and luminal pressure values ultimately resulted in the well-known FE linear system of equations[35]:

$$K_i u_i = f_i \quad \text{for} \quad i = 1,...,n, \tag{3}$$

where $K_i$ is the $m \times m$ tangent stiffness matrix of the linearized FE system, $f_i$ is the $m \times 1$ load column vector corresponding to a given set of material parameters and the discrete luminal pressure at which the system was linearized, and $u_i$ is the $m \times 1$ displacement column vector for which the linearized system is solved. The integer $m$ represents the number of degrees of freedom. We stored the final Newton–Raphson iterations that provided the final solutions for each set of parameters and luminal pressure values into $n$ vectors, $\{u_1, u_2, ..., u_n\}$, each belonging to $\mathbb{R}^m$. This set of vectors was then used to build and train the ROM as described in the next section.

The vaginal tissue was meshed in Abaqus using a structured scheme with second-order quadratic hexahedral elements (C3D20). A mesh convergence study was performed via $h$-refinement with the maximum element size ranging from 4 to .2 mm. For our convergence study, we considered a single parameter set, denoted $\mu_1$ in Table 1, for which the mean preferred fiber directions were defined by $\beta_d = \beta_m = 35°$ and $\beta_p = 55°$, and the luminal pressure was set to 75 kPa. Meshes of different sizes were compared in our convergence study using the mesh energy, $E^h$, for each maximum element size, $h$, given by

$$E^h = \frac{1}{2} \left( u^{h\top} K^h u^h \right), \tag{4}$$

where $u^h$ is the $m \times 1$ displacement column vector, and $K^h$ is the $m \times m$ tangent stiffness matrix of the linearized system for our chosen material parameters and luminal pressure. The matrices $K^h$ and vectors $u^h$ are recorded from the last Newton iteration of a solution for a given parameter set and mesh size. To assess convergence, we calculate the relative mesh energy norm error as follows:

$$\mathcal{E}(E^h) = \frac{|E^h - E^{h_{min}}|}{|E^{h_{min}}|}, \tag{5}$$

where $E^{h_{min}}$ is the mesh energy for the mesh with the smallest maximum element size in the convergence study (in our case, $h = .2$ mm) which is used as a benchmark against which all other mesh energies, $E^h$, are compared.
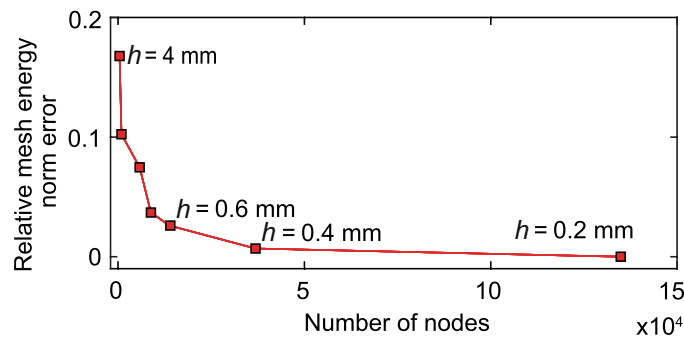


**FIGURE 3** Mesh convergence study via $h$-refinement using mean preferred fiber orientations given by $\beta_d = \beta_m = 35°$ and $\beta_p = 55°$ and luminal pressure $p_{30} = 75$ kPa. The relative mesh energy norm error is calculated as the relative error in the mesh energy for a given mesh size with respect to the mesh energy of finest mesh size ($h = .2$ mm).

The relative mesh energy norm error values are plotted against the number of nodes for the respective mesh sizes in Figure 3. Mesh convergence was considered achieved at $h = .6$ mm, where the relative mesh energy norm error was 2.6% relative to the $h = .2$ mm mesh. While we could have used a slightly finer mesh than $h = .6$ mm, anything more refined would have drastically increased computational cost for a negligible improvement in accuracy. For example, the FE simulation for our chosen parameter using a mesh with $h = .4$ mm (Figure 3) had a relative mesh energy norm error of .7% but took 451 s to complete compared to 144.7 s for $h = .6$ mm. Given the diminishing returns on relative mesh energy norm error improvements and the large increases in computational cost for meshes more refined than $h = .6$ mm, we chose $h = .6$ mm as the maximum element size for the FOM simulations used to produce our training data. The final mesh contained 672 elements and 4864 nodes. Since each node had 3 degrees of freedom, the total number of linear systems in Equations (3) was $m = 14{,}592$.

## 3 | REDUCED ORDER MODEL

In this section, we outline the construction of the standard Galerkin ROM (G-ROM) for the linear systems in Equations (3) (Section 3.1). We also construct the data-driven variational multiscale ROM (DD-VMS-ROM), which introduces a correction term to account for the effect of the discarded ROM modes and increase the ROM accuracy (Section 3.2). Moreover, we describe the criteria used to assess both the G-ROM and the DD-VMS-ROM performance.

### 3.1 | Galerkin-ROM

In this section, we briefly describe the construction of the standard Galerkin ROM, which is based on the Galerkin method. First, we use the POD method[9] to determine an orthonormal basis, the POD basis $\{\boldsymbol{\psi}_i\}_{i=1}^l$ of dimension $l$, $l \leq \min\{m, n\}$, for the set spanned by $n$ vectors, $\{\boldsymbol{u}_1, \boldsymbol{u}_2, ..., \boldsymbol{u}_n\}$, each belonging to $\mathbb{R}^m$. These vectors will be referred to as the snapshots. Specifically, we solve the following straightforward minimization problem to find the POD basis $\{\boldsymbol{\psi}_i\}_{i=1}^l$ of dimension $l$[9]:

$$\min_{\{\boldsymbol{\psi}_1, ..., \boldsymbol{\psi}_l\}} \sum_{j=1}^n \left\| \boldsymbol{u}_j - \sum_{i=1}^l \langle \boldsymbol{u}_j, \ \boldsymbol{\psi}_i \rangle_{\mathbb{R}^m} \boldsymbol{\psi}_i \right\|_2^{\mathbb{R}^m} \tag{6}$$

$$\text{subject to} \quad \langle \boldsymbol{\psi}_i, \boldsymbol{\psi}_j \rangle_{\mathbb{R}^m} = \delta_{ij} \quad \text{for} \quad 1 \leq i,j \leq l \ . \tag{7}$$

In the above equations, $\langle \cdot, \ \cdot \rangle_{\mathbb{R}^m}$ denotes the inner product in $\mathbb{R}^m$ and $\|\cdot\|_{\mathbb{R}^m} = \sqrt{\langle \cdot, \ \cdot \rangle_{\mathbb{R}^m}}$ denotes the corresponding canonical norm. Let $\boldsymbol{U}$ be the $m \times n$ matrix whose columns are the snapshots: $\boldsymbol{U} = [\boldsymbol{u}_1, ..., \boldsymbol{u}_n]$. Let $d \leq \min\{m, n\}$ be the rank of $\boldsymbol{U}$. It can be shown that the above minimization problem reduces to the solution of the following eigenvalue problem[9]:

$$\boldsymbol{U}\boldsymbol{U}^\top \boldsymbol{\psi}_i = \lambda_i \boldsymbol{\psi}_i \quad \text{for} \quad i = 1,...,d \ . \tag{8}$$

Thus, the POD basis $\{\boldsymbol{\psi}_i\}_{i=1}^l$ of dimension $l$ can be computed by solving the symmetric $m \times m$ eigenvalue problem in Equations (8). We note that the POD basis could be solved more efficiently by using the method of snapshots[36] but, even without using this method, the POD basis was quickly computed by solving the eigenvalue problem in Equations (8). Although there are no generally accepted rules on how $l$ must be selected, a popular choice is to use the relative information content (RIC) index,[37] which is the ratio of the modeled to the total energy contained in the system $\boldsymbol{U}$:

$$\mathcal{E} = \frac{\sum_{i=1}^l \lambda_i}{\sum_{i=1}^d \lambda_i} \ . \tag{9}$$

Let $\boldsymbol{\Psi}$ be the $m \times l$ matrix whose columns are the POD basis vectors: $\boldsymbol{\Psi} = [\boldsymbol{\psi}_1, ..., \boldsymbol{\psi}_l]$. The $m \times 1$ column vector $\boldsymbol{u}_i$ can be approximated by $m \times 1$ column vector

$$\boldsymbol{u}_i^{ROM} = \boldsymbol{\Psi}\boldsymbol{\zeta}_i, \quad \text{for} \quad i = 1,...,n , \tag{10}$$

where $\boldsymbol{\zeta}_i$ is an unknown $l \times 1$ column vector which must be solved for. The substitution of the $\boldsymbol{u}_i^{ROM}$ into the FE system of Equations (3) yields:

$$\boldsymbol{K}_i \boldsymbol{\Psi}\boldsymbol{\zeta}_i = \boldsymbol{f}_i \quad \text{for} \quad i = 1,...,n . \tag{11}$$

By multiplying both sides of Equations (11) by $\boldsymbol{\Psi}^\top$, we obtain the Galerkin ROM (G-ROM):

$$\boldsymbol{\Psi}^\top \boldsymbol{K}_i \boldsymbol{\Psi}\boldsymbol{\zeta}_i = \boldsymbol{\Psi}^\top \boldsymbol{f}_i \quad \text{for} \quad i = 1,...,n . \tag{12}$$

On the left side of Equations (12), $\boldsymbol{\Psi}^\top \boldsymbol{K}_i \boldsymbol{\Psi}$ is an $l \times l$ matrix, and, on the right side, $\boldsymbol{\Psi}^\top \boldsymbol{f}_i$ is an $l \times 1$ column vector. Subsequently, Equations (12) can be solved to find an $l \times 1$ column vector, $\boldsymbol{\zeta}_i$. Thus, the large, $m$-dimensional FOM system of Equations (3) has been reduced to the much lower $l$-dimensional G-ROM system of Equations (12) ($l \ll m$). This, in turn, implies that the computational cost to solve the G-ROM system of equations is significantly lower than the computational cost to solve the FOM system of equations.

To evaluate the ROM performance, we use the relative Frobenius norm of the error, $\mathcal{E}$, calculated over all the mesh points. Specifically, we use the following formula:

$$\mathcal{E} = \sqrt{\sum_{i=1}^{n} \frac{\left\| \boldsymbol{u}_i^{ROM} - \sum_{j=1}^{l} \langle \boldsymbol{u}_i^{FOM}, \ \boldsymbol{\psi}_j \rangle_{\mathbb{R}^m} \boldsymbol{\psi}_j \right\|_{\mathbb{R}^m}^2}{\left\| \sum_{j=1}^{l} \langle \boldsymbol{u}_i^{FOM}, \ \boldsymbol{\psi}_j \rangle_{\mathbb{R}^m} \boldsymbol{\psi}_j \right\|_{\mathbb{R}^m}^2}} \tag{13}$$

where $\boldsymbol{u}_i^{ROM}$ is the ROM approximation of the FOM displacement corresponding to the $i$-th parameter set which is determined via Equations (10) using $\boldsymbol{\zeta}_i$ solved for in Equations (12).

*Remark* 1. To construct the G-ROM in Equations (12), we start with the linear system in Equations (3), that is, the linear system obtained at the final iteration in the Newton–Raphson method applied to the nonlinear system of equations that result from our boundary value problem. Thus, the resulting G-ROM in Equations (12) form a low-dimensional linear system that can be efficiently solved in the online stage. Of course, this efficiency only applies to the reconstructive regime that we consider in this investigation, that is, when testing is carried out for the same parameter values as those used to train the model. We plan to extend our approach to the predictive regime in a future study.

## 3.2 | Data-driven variational multiscale ROM

ROM closure models are correction terms that are added to the classical G-ROM in order to increase its accuracy. The ROM closure models aim at representing the effect of the discarded ROM basis functions $\{\boldsymbol{\psi}_{l+1}, ..., \boldsymbol{\psi}_d\}$ on the ROM displacement solutions in the low-dimensional space spanned by the ROM basis functions $\{\boldsymbol{\psi}_1, ..., \boldsymbol{\psi}_l\}$. In computational fluid dynamics, the ROM closure models can significantly increase the ROM accuracy (see the survey in reference [37]). To our knowledge, there are no ROM closure models for solid mechanics and, in this section; we take a first step to fill this gap.

To construct the ROM closure model, we utilize DD algorithms and leverage the hierarchical structure of the POD basis within a variational multiscale (VMS) framework.[38,39] Specifically, we extend the DD-VMS-ROM framework from fluid flows[40–42] to soft biological tissues. To this end, in addition to the $m \times l$ matrix $\boldsymbol{\Psi}$ defined in Equations (10), where $d > l$, we consider the $m \times (d - l)$ matrix $\boldsymbol{\Psi}'$, which contains the ROM basis functions $\{\boldsymbol{\psi}_{l+1}, ..., \boldsymbol{\psi}_d\}$. Thus, if we replace the ansatz for the ROM deformation solution in Equations (10) with

$$\boldsymbol{u}_i^{ROM} = \boldsymbol{\Psi}\boldsymbol{\zeta}_i + \boldsymbol{\Psi}'\boldsymbol{\zeta}_i' \quad \text{for} \quad i = 1,...,n , \tag{14}$$

where $\zeta_i'$ is an unknown $(d-l) \times 1$ column vector corresponding to $\Psi'$, we expect a more accurate ROM approximation of the displacement solution. Substituting the ROM solutions (14) into the FE Equations (3), we obtain

$$K_i \Psi \zeta_i + K_i \Psi' \zeta_i' = f_i \quad \text{for} \quad i = 1,...,n . \tag{15}$$

Next, we perform a Galerkin projection of Equation (15) onto the space spanned by the POD basis $\{\psi_i\}_{i=1}^l$, that is, we multiply Equations (15) by $\Psi^\top$:

$$\left(\Psi^\top K_i \Psi\right)\zeta_i + \left(\Psi^\top K_i \Psi'\right)\zeta_i' = \Psi^\top f_i \quad \text{for} \quad i = 1,...,n . \tag{16}$$

Of course, since we use more ROM basis functions (and unknowns in $\zeta_i'$) in Equations (16) than in Equations (12), we expect the former to yield a more accurate solution than the latter. We want, however, to maintain a low computational cost, similar to the computational cost of the G-ROM in Equations (12). To this end, we make the following ansatz:

$$\left(\Psi^\top K_i \Psi'\right)\zeta_i' \approx A\zeta_i + \zeta_i^\top B\zeta_i \quad \text{for} \quad i = 1,...,n , \tag{17}$$

where $A$ is an $l \times l$ matrix and $B$ is an $l \times l \times l$ array that need to be determined.

*Remark* 2. Since the starting point in the DD-VMS-ROM construction is the FE linear system in Equations (3), our choice of a quadratic ansatz in Equations (17) needs to be explained. Our initial choice was a linear ansatz, that is, $\left(\Psi^\top K_i \Psi'\right)\zeta_i' \approx A\zeta_i$. However, in our numerical investigation, the linear ansatz did not produce meaningful results, providing a matrix $A$ with zero entries. Thus, the numerical results suggested that the linear ansatz is simply not capable of providing a good approximation of our data. To address this issue, we decided to replace the more natural linear ansatz with the quadratic ansatz in Equations (17), which yielded nonzero entries both in $A$ and in $B$. We note that, although the elements of $A$ were nonzero when the quadratic ansatz was used, they were still much smaller than the elements of $B$, suggesting that the linear term contributed relatively little to the solution.

We also note that, although the DD-VMS-ROM construction is based on the FE linear system in Equations (3), this linear system represents just the final iteration in the Newton–Raphson method used to solve the nonlinear boundary value problem that describes the deformations of the vaginal tissue under pressure. Thus, using a nonlinear (quadratic) ansatz in this context seems justified. Furthermore, we note that the quadratic ansatz selected here is typical in computational fluid dynamics as it mimics the nonlinear operator in the Navier–Stokes equations. However, other nonlinear operators appear in the governing equations of anisotropic nonlinear elastic materials described by Equations (1)–(2). In this study, we chose a quadratic ansatz for simplicity but one should investigate the use of other nonlinear ansatzes for the DD-VMS-ROMs. Finally, we note that we plan to implement a fully nonlinear G-ROM with the selection of a nonlinear ansatz for the DD-VMS-ROM in future. In that case, the DD-VMS-ROM would likely not have a significantly greater computational cost than the G-ROM.

Substituting the ansatz in Equations (17) into Equations (16), we obtain the DD-VMS-ROM:

$$\left(\Psi^\top K_i \Psi\right)\zeta_i' + A\zeta_i + \zeta_i^\top B\zeta_i = \Psi^\top f_i, \quad \text{for} \quad i = 1,...,n. \tag{18}$$

The DD-VMS-ROM in Equations (18), like the G-ROM in Equations (12), is solved for the unknowns in $\zeta_i$, but yields a more accurate approximation when $\zeta_i$ is substituted into Equations (10) since it includes a model for the unknowns in $\zeta_i'$. We also note that the DD-VMS-ROM in Equations (12) is a nonlinear (quadratic) system of equations in the unknown $\zeta_i$. This is in contrast with the G-ROM in Equations (12), which is a linear system of equations. To solve the nonlinear system of Equations in (18), we use the Newton–Raphson method.

To construct $A$ and $B$ in the DD-VMS-ROM in Equations (18), we use DD modeling[43] and solve the following least squares problem:

$$\min_{A \in \mathbb{R}^{l \times l}, B \in \mathbb{R}^{l \times l}} \sum_{i=1}^{n} \left\| \left( \boldsymbol{\Psi}^T \boldsymbol{K}_i \boldsymbol{\Psi}' \right) \boldsymbol{\zeta}_i'^{FOM} - A \boldsymbol{\zeta}_i^{FOM} - \boldsymbol{\zeta}_i^{FOM^T} B \boldsymbol{\zeta}_i^{FOM} \right\|_{\mathbb{R}^m}^2, \tag{19}$$

where $\boldsymbol{\zeta}_i'^{FOM}$ and $\boldsymbol{\zeta}_i^{FOM}$ are computed from the FOM (i.e., FE) numerical approximation. Specifically, we set

$$\boldsymbol{u}_i^{FOM} = \boldsymbol{\Psi} \boldsymbol{\zeta}_i^{FOM} + \boldsymbol{\Psi}' \boldsymbol{\zeta}_i'^{FOM} \quad \text{for} \quad i = 1,...,n, \tag{20}$$

multiply Equations (20) to the left by $\boldsymbol{\Psi}^\top$ and $\boldsymbol{\Psi}'^\top$, use the orthonormality of the ROM basis functions (i.e., $\boldsymbol{\Psi}^\top \boldsymbol{\Psi} = \boldsymbol{I}$, $\boldsymbol{\Psi}^\top \boldsymbol{\Psi}' = \boldsymbol{0}$, $\boldsymbol{\Psi}'^\top \boldsymbol{\Psi} = \boldsymbol{0}$, and $\boldsymbol{\Psi}'^\top \boldsymbol{\Psi}' = \boldsymbol{I}$), and finally obtain

$$\boldsymbol{\zeta}_i^{FOM} = \boldsymbol{\Psi}^\top \boldsymbol{u}_i^{FOM} \quad \text{for} \quad i = 1,...,n, \tag{21}$$

$$\boldsymbol{\zeta}_i'^{FOM} = \boldsymbol{\Psi}'^\top \boldsymbol{u}_i^{FOM} \quad \text{for} \quad i = 1,...,n. \tag{22}$$

The solution of the least squares problem in Equations (19) can be obtained using Algorithm 1.[41]

In summary, we use Algorithm 1 to solve the least squares problem in Equation (19) and obtain $A$ and $B$ in the offline stage and then we use the DD-VMS-ROM in Equations (18) with the computed $A$ and $B$ in the online stage.

We note that the dimension of the quadratic (nonlinear) system in the DD-VMS-ROM in Equations (18) is the same as the dimension of the linear system of the G-ROM in Equations (12), that is, we solve $l$ equations with $l$ unknowns, where $l$ is relatively small. Thus, we expect that the online computational costs of the DD-VMS-ROM and G-ROM are of the same order. We emphasize, however, that since the DD-VMS-ROM in Equations (18) includes the computation of the matrix $A$ and the array $B$ that model the effect of the unknowns in $\boldsymbol{\zeta}'$, we expect the DD-VMS-ROM to be more accurate than the G-ROM.

To evaluate the DD-VMS-ROM performance, we again use the relative Frobenius norm of the error. Specifically, we substitute the solution $\boldsymbol{\zeta}_i$ from Equation (18) into Equation (10) to determine the ROM approximation, $\boldsymbol{u}_i^{ROM}$, which we then use in Equation (13) to calculate $\mathcal{E}$.

## 3.2.1 | Ideal ROM

As a benchmark for the performance of the DD-VMS-ROM, we employ the ideal ROM (I-ROM), which is a theoretical model that represents the best possible performance of the DD-VMS-ROM. To construct the I-ROM, we consider the DD-VMS-ROM framework starting from Equations (16).

However, instead of using the ansatz in Equation (17) to approximate $\left( \boldsymbol{\Psi}^\top \boldsymbol{K}_i \boldsymbol{\Psi}' \right) \boldsymbol{\zeta}_i'$ in terms of $\boldsymbol{\zeta}_i$, we substitute $\boldsymbol{\zeta}_i'^{FOM}$ in place of $\boldsymbol{\zeta}_i'$ to obtain the I-ROM closure model:

$$\left( \boldsymbol{\Psi}^\top \boldsymbol{K}_i \boldsymbol{\Psi} \right) \boldsymbol{\zeta}_i + \left( \boldsymbol{\Psi}^\top \boldsymbol{K}_i \boldsymbol{\Psi}' \right) \boldsymbol{\zeta}_i'^{FOM} = \boldsymbol{\Psi}^\top \boldsymbol{f}_i, \quad \text{for} \quad i = 1,...,n. \tag{28}$$

Thus, in the I-ROM in Equations (28) we solve for the unknowns in $\boldsymbol{\zeta}_i$ without needing to construct $A$ and $B$. The approximation, $\boldsymbol{u}_i^{ROM}$, obtained by substituting $\boldsymbol{\zeta}_i$ from Equations (28) into Equations (10) can then act as a reference to determine how well the DD-VMS-ROM performed compared to what is theoretically achievable. As with the other ROM approaches, the performance of the I-ROM is determined by substituting $\boldsymbol{u}_i^{ROM}$ in Equations (13) to calculate the relative Frobenius norm error. We emphasize again that the I-ROM in Equations (28) is just an idealized/theoretical model that cannot be used in practice since it relies on $\boldsymbol{\zeta}_i'^{FOM}$, which is not generally known.

**ALGORITHM 1**

1: Following,[41] rewrite the optimization problem in Equation (19) as the following least squares problem:

$$\min_{\boldsymbol{x} \in \mathbb{R}^{l^2+l^3}} \|\boldsymbol{E}\boldsymbol{x} - \boldsymbol{d}\|^2_{\mathbb{R}^{nl}}, \tag{23}$$

where $\boldsymbol{E}$ is an $nl \times (l^2 + l^3)$ matrix constructed from $\boldsymbol{\zeta}_i^{FOM}$, $\boldsymbol{d}$ is an $nl \times 1$ column vector constructed from $(\boldsymbol{\Psi}^\top \mathbf{K}_i \boldsymbol{\Psi}') \zeta_i'^{FOM}$, and $\boldsymbol{x}$ is an unknown $(l^2 + l^3) \times 1$ column vector defined in terms of the entries of $\boldsymbol{A}$ and $\boldsymbol{B}$.

2: Use the truncated SVD algorithm to solve the linear least squares problem in Equation (23). Specifically

    i. Calculate the SVD of $\boldsymbol{E}$:

$$\boldsymbol{E} = \boldsymbol{U}\boldsymbol{\Sigma}\boldsymbol{V}^\top, \tag{24}$$

    where $\boldsymbol{U}$ is an $nl \times nl$ orthogonal matrix, $\boldsymbol{\Sigma}$ is a $nl \times (l^2 + l^3)$ rectangular diagonal matrix, and $\boldsymbol{V}$ is an $(l^2 + l^3) \times (l^2 + l^3)$ orthogonal matrix. Let $m$ be the rank of matrix $\boldsymbol{E}$ (and $\boldsymbol{\Sigma}$) and let $\sigma_j$ for $j = 1, ..., m$, be the diagonal entries of $\boldsymbol{\Sigma}$.

    ii. For $j = 1, ..., m$, select a tolerance $\sigma_{tol}^{(j)} = \sigma_j$.

        (a) For each $\sigma_{tol}^{(j)}$, construct a new diagonal matrix $\widehat{\boldsymbol{\Sigma}}^{(j)}$ by setting its diagonal entries to be equal to the diagonal entries of $\boldsymbol{\Sigma}$, i.e., $\widehat{\sigma}_k = \sigma_k$, when $\sigma_k \geq \sigma_{tol}^{(j)}$ with $k = 1, ..., m$.

        (b) For each $\sigma_{tol}^{(j)}$, construct the truncated SVD of $\boldsymbol{E}$, $\widehat{\boldsymbol{E}}^{(j)}$, by setting

$$\widehat{\boldsymbol{E}}^{(j)} = \widehat{\boldsymbol{U}}^{(j)} \widehat{\boldsymbol{\Sigma}}^{(j)} \widehat{\boldsymbol{V}}^{(j)\top}, \tag{25}$$

where $\widehat{\boldsymbol{U}}^{(j)}$ has the column vectors of $\boldsymbol{U}$ and $\widehat{\boldsymbol{V}}^{(j)}$ has the row vectors of $\boldsymbol{V}$ corresponding to $\widehat{\boldsymbol{\Sigma}}^{(j)}$.

        (c) For each $\sigma_{tol}^{(j)}$, the solution of the least squares problem in Equations (23) is

$$\boldsymbol{x}^{(j)} = \widehat{\boldsymbol{V}}^{(j)} \widehat{\boldsymbol{\Sigma}}^{(j)-1} \widehat{\boldsymbol{U}}^{(j)\top} \boldsymbol{d}. \tag{26}$$

        (d) For each $\sigma_{tol}^{(j)}$, solve the resulting DD-VMS-ROM in Equations (18), with the entries of $\boldsymbol{A}^{(j)}$ and $\boldsymbol{B}^{(j)}$ computed from $\boldsymbol{x}^{(j)}$, and calculate the average error, $\mathcal{E}^{(j)}$, by using formula in Equation (13).

    iii. Select the optimal $\widetilde{j}$ (and corresponding $\sigma_{tol}^{(\widetilde{j})}$) such that

$$\mathcal{E}^{(\widetilde{j})} = \min_{j=1,...,m} \mathcal{E}^{(j)}, \tag{27}$$

and select the corresponding optimal $\boldsymbol{x}^{(\widetilde{j})}$ from which the optimal entries of $\boldsymbol{A}^{(\widetilde{j})}$ and $\boldsymbol{B}^{(\widetilde{j})}$ are computed.

# 4 | RESULTS

The FOM solutions (snapshots) that were used to create the POD basis for the ROMs described a diverse set of deformations experienced by the vaginal tissue under pressure. These solutions varied with changes in luminal pressure, $p_1$, ..., $p_{30}$, and changes in collagen fiber orientation defined by $\beta_p$, $\beta_m$, and $\beta_d$ in the proximal, mid, and distal vagina, respectively. As expected, the magnitude of the displacement field increased as the applied internal pressure increased, for each fiber orientation set considered (Figure 4). Variations in the magnitude of the displacement field for FOM solutions obtained for various collagen fiber orientation sets were also observed. These solutions resulted in different shapes of the deformed geometries at the same applied internal pressure (Figure 5). This was expected, as a change in fiber orientation from $\beta_d = 25°$ to $\beta_d = 35°$ in the distal region and from $\beta_m = 25°$ to $\beta_m = 35°$ in the mid region would change the mechanical response of either region by making it more compliant in the hoop direction. Similarly, a change in the proximal region from $\beta_p = 55°$ to $\beta_p = 65°$ would make the tissue slightly stiffer in the axial direction. Thus, the mid and distal regions of the vagina deformed in a more prolate-like shape when their fibers were oriented at 25°, and the proximal region deformed in a more prolate-like shape when the fibers were oriented at 65°. The model depicted in Figure 5B differed from that in Figure 5A by its mid region fiber orientation of $\beta_m = 35°$, which resulted in greater deformation and thus a rounder shape through the mid region at the same luminal pressure. Both the distal and proximal regional fiber orientations of the model in Figure 5C differed from those of Figure 5A with $\beta_d = 35°$ and $\beta_p = 55°$. These differences resulted in a relative increase in the magnitude of displacement in the distal region and a relative decrease in the magnitude of the displacement in the proximal region for the model of Figure 5C compared to the model in Figure 5A under the same luminal pressure, whereas the mid regions of both are similar in terms of displacement magnitude. Consequently, the overall model in Figure 5C is rounder on the distal end and comparatively prolate on its proximal end. Lastly, Figure 5D depicts an FE solution with fiber orientations that are entirely different from those for the solution in Figure 5A. With $\beta_d = \beta_m = 35°$ and $\beta_p = 55°$, the FE model in Figure 5D had relatively larger displacement magnitude in the mid and distal regions and relatively smaller displacement magnitude in the proximal region compared to the FE model in Figure 5A at the same luminal pressure. Thus, the modeled vaginal canal in Figure 5D was rounder through the mid and distal regions but more prolate in the proximal region, while the modeled vaginal canal in Figure 5A had prolate mid and distal regions and a rounder proximal region.
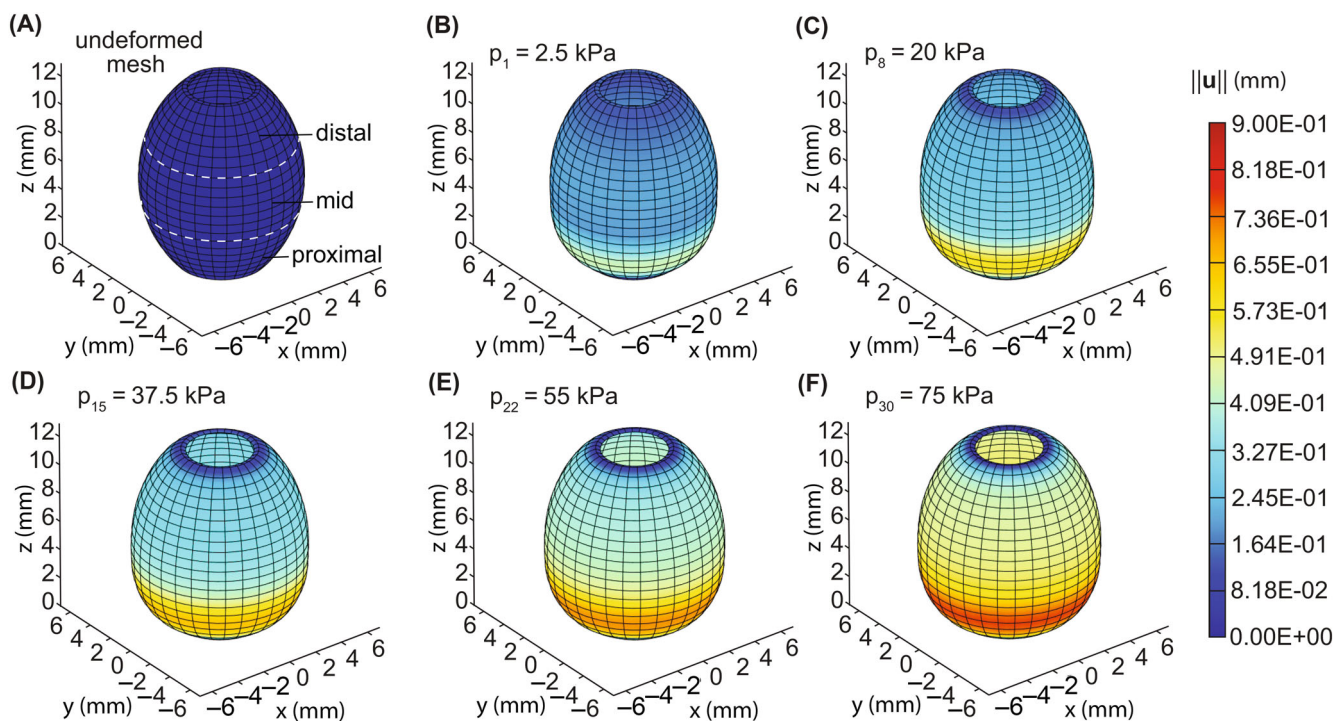


**FIGURE 4** (A) Undeformed mesh of the FE model showing the distal, mid, and proximal regions of the vagina. (B)–(D) FOM solutions for various values of the applied internal pressure $p_i$, with $\beta_d = \beta_m = 35°$ and $\beta_p = 55°$. The top, middle, and bottom in each FE model correspond to the distal, mid, and proximal anatomical regions of the vagina, respectively.
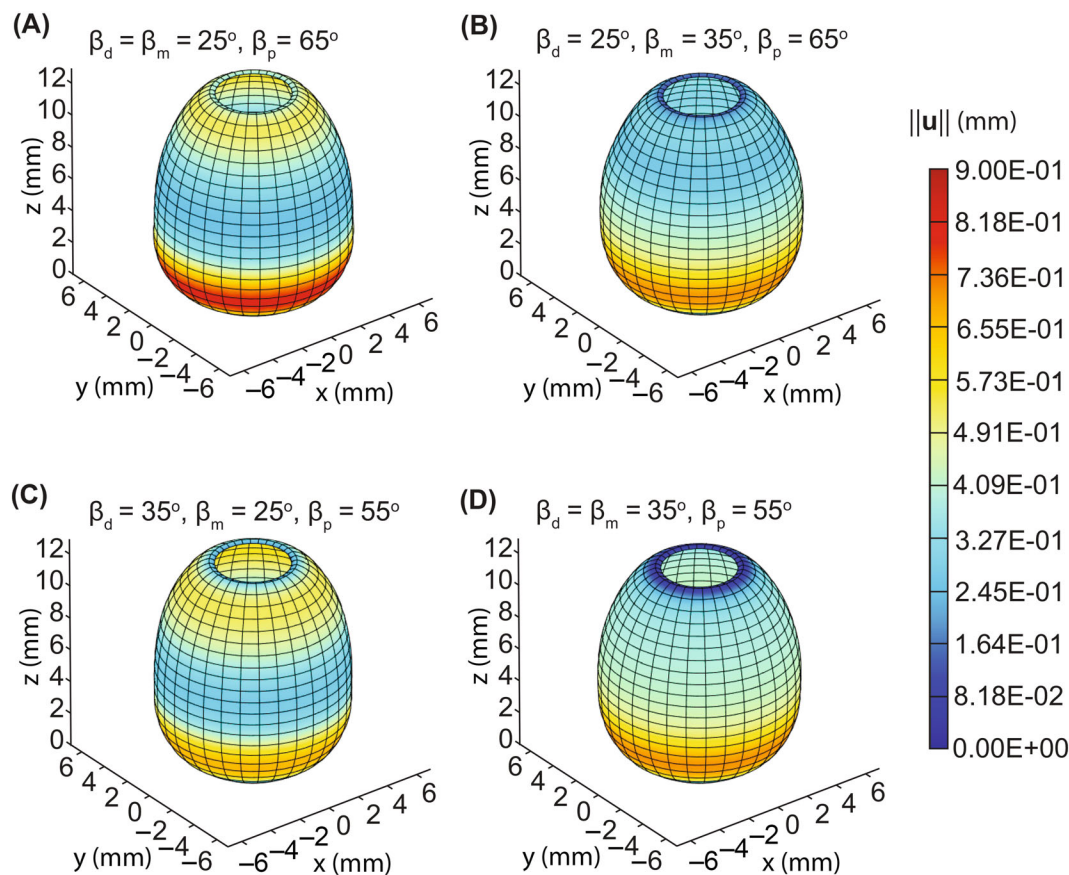
**FIGURE 5** (A)–(D) FOM solutions for various values of parameters $\beta_d$, $\beta_m$, $\beta_p$ at an applied internal pressure $p_{22} = 55$ kPa. The top, middle, and bottom in each FE model correspond to the distal, mid, and proximal anatomical regions of the vagina, respectively.
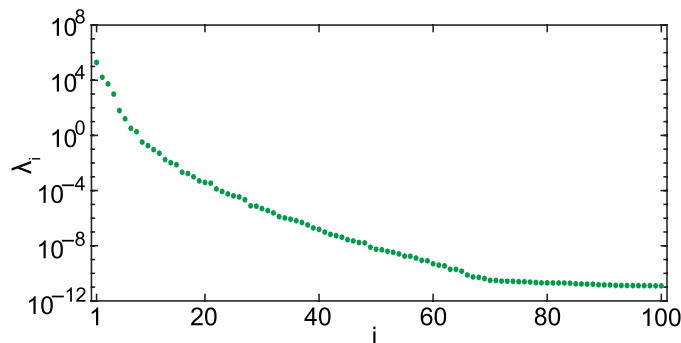


**FIGURE 6** Decay of the eigenvalues $\lambda_1, \ldots, \lambda_{100}$ corresponding to the POD basis functions $\psi_1, \ldots, \psi_{100}$, respectively.

The decay of the eigenvalues of $UU^\top$ from Equation (8) indicated that the basis functions corresponding to the gradually decreasing eigenvalues transitioned from representing major characteristics of the FOM solutions to minor features that provided little additional information about the solutions around $l = 70$. This can be seen in Figure 6, where the eigenvalues reached a plateau at values of $O(10^{-11})$ when the dimension of the ROM basis exceeded $l = 70$. We note that the first eigenvalue at $l = 1$ is $O(10^5)$, while the plateau is reached at $O(10^{-11})$. Thus, the ratio between the eigenvalues on the plateau and the first eigenvalue is $O(10^{-16})$, which is on the order of machine precision. Such a plateau in eigenvalues is generally associated with the exhaustion of viable POD basis functions, which are basis functions that, when used to build the ROMs, increase their accuracy.

This progression of basis functions, from viable to non-viable with increasing $l$, is visualized by plotting the magnitude of several POD basis functions at their corresponding nodes on the model geometry (Figure 7). The first POD basis
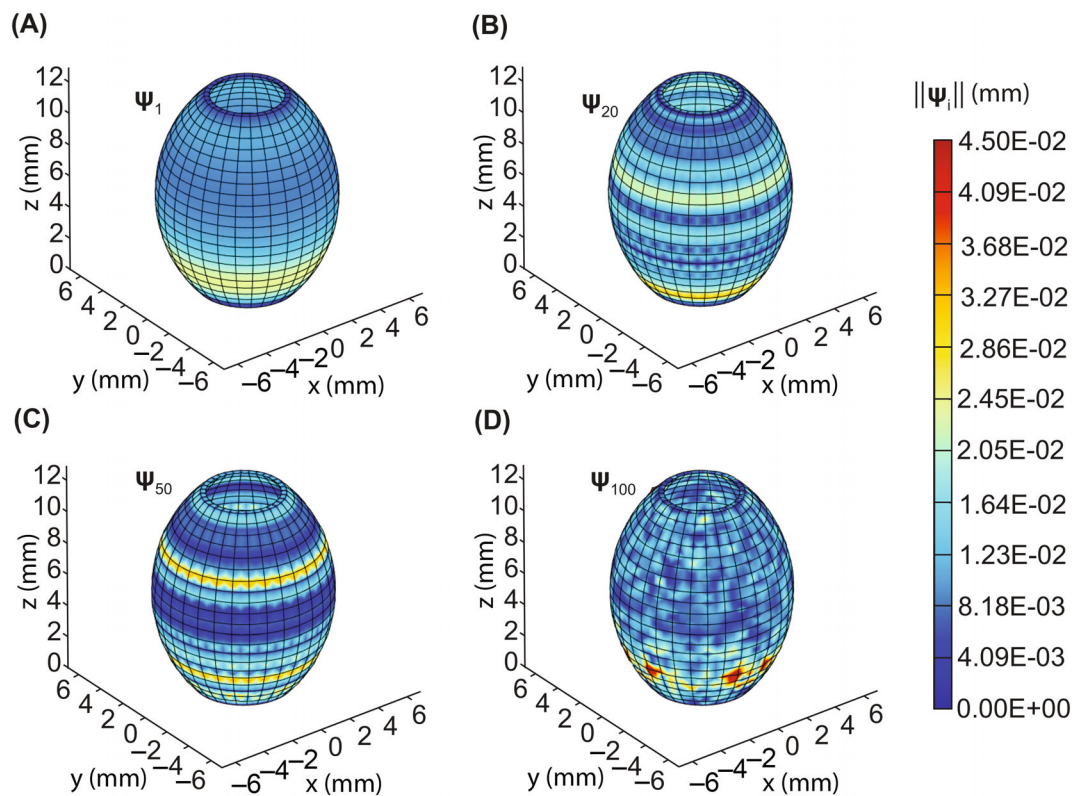
**FIGURE 7** Magnitudes of (A) 1st, (B) 20th, (C) 50th, and (D) 100th POD basis functions. The top, middle, and bottom of the deformed geometry in (A), (B), (C), and (D) correspond to the distal, mid, and proximal anatomical regions of the vagina, respectively.
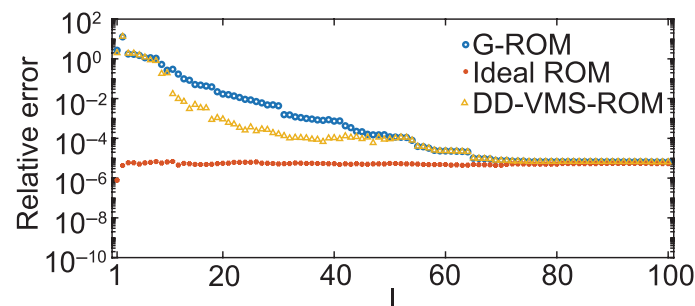


**FIGURE 8** Relative error measured using the Frobenius norm as a function of the dimension of the ROM basis, $l$.

function had a magnitude field, which resembled the FOM results with the greatest magnitude values concentrated in the proximal region, the smallest magnitude values in the mid region, and slightly greater magnitude values near the uppermost opening in the distal region (Figure 7A). In contrast, the 20th and 50th POD basis functions were characterized by numerous circumferential bands of varying constant magnitudes (Figure 7B,C). Finally, the 100th POD basis function had no discernible pattern to its magnitude field (Figure 7D).

The exhaustion of viable ROM basis functions for $l > 70$ was confirmed by diminishing returns in relative Frobenius norm error improvements for the G-ROM and DD-VMS-ROM. It can be seen in Figure 8 that the error for both ROM methods asymptotically approached the theoretical performance benchmark provided by the I-ROM of relative Frobenius norm error $O(10^{-6})$ when using $l > 70$ ROM basis functions. Thus, additional basis functions beyond this threshold had a negligible impact on the accuracy of the ROM approximations.

The accuracy of the DD-VMS-ROM was comparable to that of the G-ROM up to $l = 10$ with the relative Frobenius norm errors of both being $O(10^0)$ (Figure 8). Additional ROM basis functions above this threshold yielded substantially lower error for the DD-VMS-ROM compared to the G-ROM, with the most pronounced improvements from the DD-
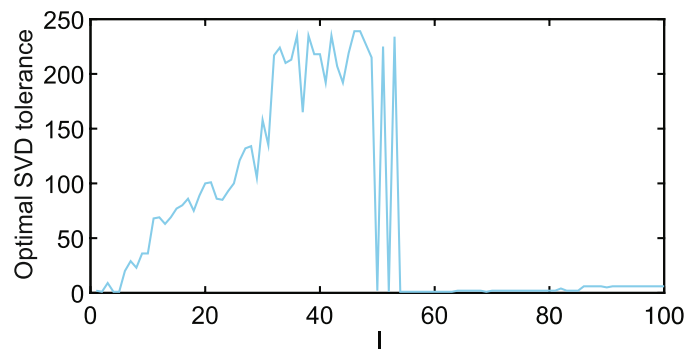
**FIGURE 9**  Optimal tolerance of the truncated SVD solver used to calculate $A$ and $B$ as a function of the number of bases, $l$.

VMS-ROM occurring between $l = 20$ and $l = 40$, where its error was consistently an order of magnitude smaller, with G-ROM errors in the range from $O(10^{-2})$ to $O(10^{-3})$ and the DD-VMS-ROM errors ranging from $O(10^{-3})$ to $O(10^{-4})$. However, the errors of the DD-VMS-ROM and the G-ROM converged and once again became comparable for $l > 50$. This convergence of errors would be expected for $l > 70$ as the additional information from the basis functions $\boldsymbol{\Psi}'$ gave the DD-VMS-ROM an advantage over the G-ROM, but only insofar as those additional basis functions contained useful information. However, this earlier convergence of error between the ROM approaches appeared to coincide with situations where the truncated SVD solver in Algorithm 1, which determined the DD-VMS-ROM correction terms $A$ and $B$, defaulted to an optimal truncation tolerance, $\sigma_{tol}^{(\tilde{j})}$, of 1 (Figure 9). This occurred when none of the possible tolerances $\sigma_{tol}^{(j)}$ for $j = 1, ..., m$ (as defined in Algorithm 1) produced correction terms which improved upon the G-ROM error. Therefore, the minimum error according to Equation (27) would occur when all but one of the singular values from the SVD of $E$ were truncated, and the limited amount of information retained from $E$ when solving Equation (26) generally caused the entries of $A$ and $B$ to be small. Thus, with correction terms whose entries were nearly equal to 0, the DD-VMS-ROM results were nearly identical to the G-ROM results. This suggests that our quadratic ansatz from Equation (17) did not hold for the ROM bases for which this behavior occurred.

In contrast to Figure 8, which presents the relative Frobenius norm of the error averaged across all nodes in our model, Figure 10 shows the relative Frobenius norm of the error at each node mapped onto the geometry of our model to illustrate error variation by region. Snapshots were chosen from four different sets of mean preferred fiber orientation angles, all with a luminal pressure of $p_{22} = 55$ kPa. The G-ROM, DD-VMS-ROM, and I-ROM approximations of these snapshots were determined using a ROM basis of dimension $l = 20$. Disparities in the magnitudes of nodal error between ROM approaches for these snapshots reflected those observed with the averaged error. However, the distribution of nodal error varied with the fiber orientation parameters resulting in circumferential bands of larger or smaller error, which were unique to each set of parameters $\beta_d$, $\beta_m$, and $\beta_p$. For instance, consider the I-ROM and G-ROM of Figure 10C. The I-ROM had the least error in the distal region and greatest error in the mid and proximal regions as well as around the boundary of the distal region. The G-ROM had smaller error in the region between the mid and distal regions as well as the proximal and distal boundaries, but it had larger error everywhere else. In the same fashion, the DD-VMS-ROM in Figure 10D shows larger error in the distal and mid regions and smaller error around the proximal boundary.

In addition to analyzing the error, we recorded the total CPU time required to complete the online stages of the G-ROM and DD-VMS-ROM simulations for comparison to the CPU time required to complete the FOM. The online stage of our ROM simulations refers to the process of solving for $\zeta_i$ and subsequently computing $\boldsymbol{u}_i^{ROM}$ for each ROM method. The construction of the ROM basis matrices, $\boldsymbol{\Psi}$ and $\boldsymbol{\Psi}'$, and other ROM quantities such as $A$, $B$, $\zeta_i^{FOM}$, and $\zeta_i^{'FOM}$, was considered part of the offline stage. The ratio of ROM CPU time to FOM CPU time is referred to as the speed-up factor (SUF) and is reported in Table 2 at 11 values of the ROM basis dimension, $l$, over the range $l = 1, ..., 100$. Initially, the DD-VMS-ROM appeared to perform comparably to the G-ROM as both SUFs were $O(10^6)$, and, at $l = 20$, the DD-VMS-ROM was even slightly faster than the G-ROM. However, as $l$ increased it was clear that the DD-VMS-ROM was the slower of the two methods, though not by much. For $l > 50$, the disparity between the two methods became more pronounced with the run-times for the DD-VMS-ROM increasing such that SUFs were $O(10^5)$ whereas the G-ROM SUFs consistently dropped to $O(10^5)$ until $l > 80$, at which point the G-ROM SUFs were still about half an order of magnitude greater than those of the DD-VMS-ROM.
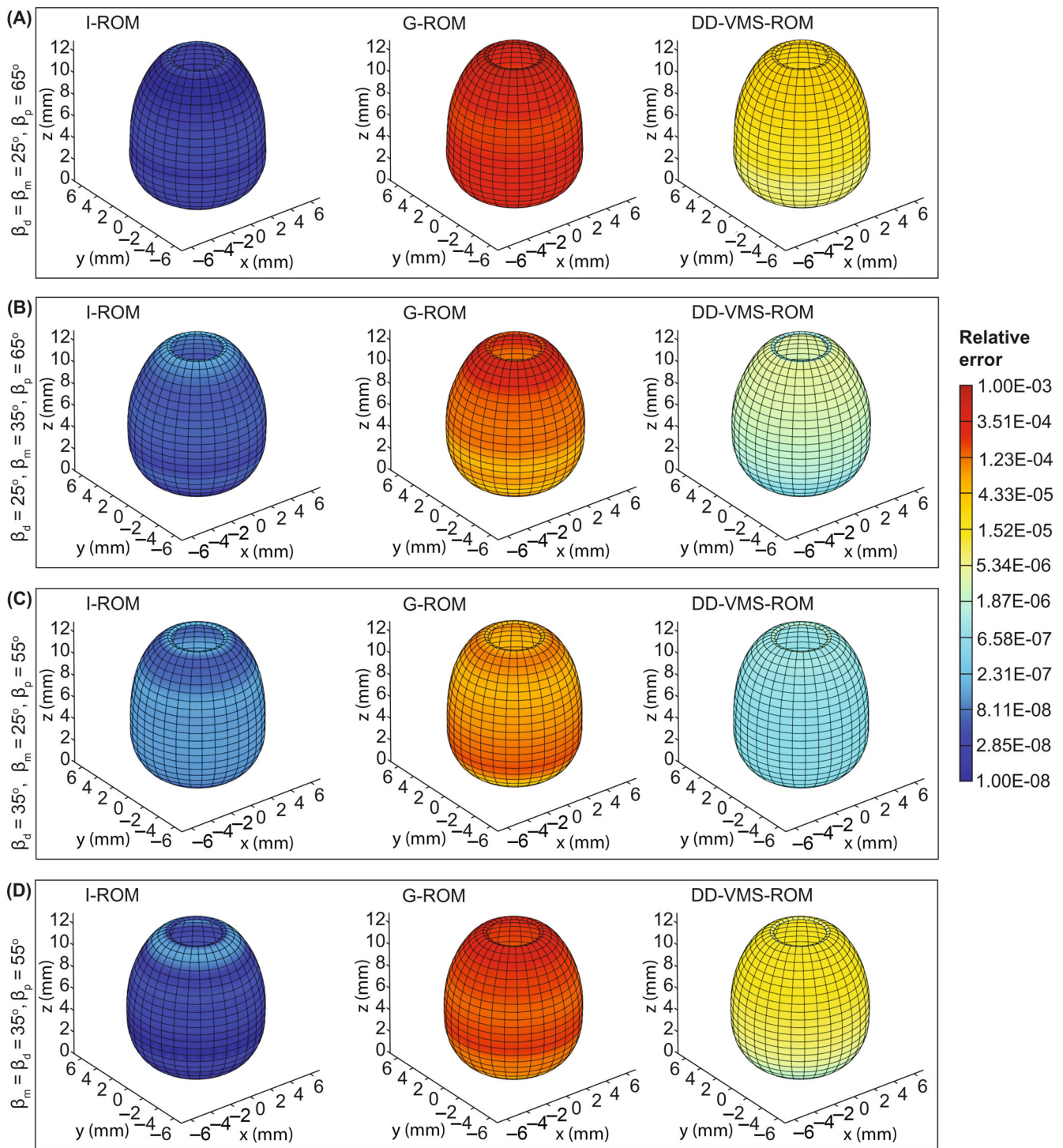
**FIGURE 10** Relative errors for I-ROM, G-ROM, and DD-VMS-ROM solutions calculated using a ROM basis of dimension $l = 20$ for different sets of $\beta_p$, $\beta_m$, and $\beta_d$ at an equal luminal pressure of $p_{22} = 55$ kPa. The top, middle, and bottom of the deformed geometry in (A), (B), (C), and (D) correspond to the distal, mid, and proximal anatomical regions of the vagina, respectively.

## 5 | DISCUSSION

This study presents a proof-of-concept for computational tools that employ ROMs to simulate the complex mechanical behavior of vaginal tissue in real-time. First, we constructed FE models based on previously collected experimental data that characterized the ex vivo biaxial response of rat vaginal tissue via inflation testing. By assuming that the vaginal tissue behaved as a nonlinear anisotropic hyperelastic material using the Holzapfel-Gasser-Ogden constitutive law, we generated FOM snapshots by changing the luminal pressure and selecting eight different parameter sets, $\mu_1, \cdots, \mu_8$, as

**TABLE 2**    SUFs for G-ROM and DD-VMS-ROM at $l = 1, ..., 100$ in intervals of 10

| $l$ | Speed-up Factor | |
| --- | --- | --- |
| | **G-ROM** | **DD-VMS-ROM** |
| $l = 1$ | $4.46 \times 10^6$ | $3.44 \times 10^6$ |
| $l = 10$ | $4.04 \times 10^6$ | $1.53 \times 10^6$ |
| $l = 20$ | $3.05 \times 10^6$ | $4.03 \times 10^6$ |
| $l = 30$ | $2.72 \times 10^6$ | $2.13 \times 10^6$ |
| $l = 40$ | $2.33 \times 10^6$ | $1.62 \times 10^6$ |
| $l = 50$ | $1.31 \times 10^6$ | $1.01 \times 10^6$ |
| $l = 60$ | $1.26 \times 10^6$ | $7.16 \times 10^5$ |
| $l = 70$ | $1.10 \times 10^6$ | $4.91 \times 10^5$ |
| $l = 80$ | $1.03 \times 10^6$ | $4.48 \times 10^5$ |
| $l = 90$ | $8.98 \times 10^5$ | $3.32 \times 10^5$ |
| $l = 100$ | $7.96 \times 10^5$ | $2.39 \times 10^5$ |

reported in Table 1, which represented different orientations of collagen fibers across the proximal, mid, and distal regions of the vagina. The FE data were then used to train the ROMs, with both the G-ROM and DD-VMS-ROM approximations demonstrating exceptional online time-savings compared to the FOM (Table 2). Even for our most expensive ROM simulations (i.e., $l = 100$), where the relative Frobenius norm errors of both the G-ROM and the DD-VMS-ROM were $O(10^{-6})$ (Figure 8), we achieved SUFs of $O(10^5)$. Most notable, however, was the performance of the DD-VMS-ROM for ROM bases of dimension $l = 20,...,40$. In this range, the DD-VMS-ROM had an error that ranged from $O(10^{-3})$ to $O(10^{-4})$, which was consistently one order of magnitude smaller than the error for the G-ROM. Over the same range, the DD-VMS-ROM had SUFs of $O(10^6)$ and so was comparable to the G-ROM in terms of computational cost. This represents the optimal use-case for ROM bases of certain dimensions, where the DD-VMS-ROM provides superior accuracy to the G-ROM without sacrificing the speed of calculations, which is necessary for real-time applications.

The pre-loaded ex vivo rat vagina was assumed to be a fairly simple hollow prolate spheroid with rotational symmetry. This assumption on the geometry of the organ, with three distinct anatomical regions, provided enough complexity to test our ROM approaches in terms of accuracy and time-savings (Figure 1). Of course, we could have reduced the FOM and ROM computational cost further by assuming that the organ was 2-D axisymmetric rather than using a fully 3-D model. However, our goal was not to reduce computational costs for the FOM but to build a framework for the general application of ROM to FE models with complex geometry, boundary conditions, and constitutive behavior. In other words, the goal of this investigation was not to make a simple problem complex in order to then make it efficient again with ROMs, but to demonstrate robustness of ROM methods for such complexity, albeit on a problem that could have been mathematically modeled much more simply. In the future, one should build FE models of the vagina with geometry and boundary conditions that better replicate the in vivo conditions of the organ. Indeed, it is well known that the vaginal canal is not axisymmetric and, within the pelvic floors, it is subjected to forces exerted by the surrounding connective tissues and intra-abdominal pressure.

Together with a realistic geometry, boundary and loading conditions, a new constitutive law that accounts for the experimentally measured statistical distributions of collagen fibers[32] and smooth muscle fibers[44] should be developed for the rat vagina. The specific form of the Holzapfel-Gasser-Ogden constitutive model used in this study does not consider the exact distributions of such fibers in the rat vagina. However, despite this and other limitations (e.g., neglected contribution of compressed fibers), we elected to adopt this well-established model in biomechanics since it is already in the constitutive library of *Abaqus* and, thus, can be easily implemented by other researchers working in reproductive biomechanics. We acknowledge that more advanced constitutive formulations should be employed to account for the contribution of the dispersed fibers within the vaginal tissue. For example, one could define the strain energy density by introducing a statistical distribution of collagen and smooth muscle fibers, the undulation of such fibers, and the interaction of the fibers with the surrounding matrix.[45] However, this approach requires expensive numerical integrations. One notable and alternative approach that preserves the computational efficiency of the Holzapfel-Gasser-Ogden

constitutive model consists in defining an energy density function that depends not only on the average value of the pseudo-invariant $\bar{I}_{4(\alpha\alpha)}$ but also on the variance of the same pseudo-invariant.[46,47] Moreover, future constitutive models should also capture the mechanical response of the vagina in the both the relaxed and contracted states.[48–50]

The material parameters in the Holzapfel-Gasser-Ogden constitutive model were chosen such that the average pressure-strain curves in the hoop and axial directions were within the range of those that we computed experimentally (Figure 2). During our inflation experiments,[31] the strains were calculated in the mid region of the rat vagina using the digital image correlation method. For consistence, the average pressure-strain relations that were derived from the FE simulations were relative to the mid region of the modeled organ. For this reason, the selected parameters, especially those that describe the collagen fiber organization of the vagina in the proximal and distal regions, may not be adequate to capture the mechanical behavior of the entire rat vagina. Because of the variation in the collagen fiber organization in the three main anatomical regions of the organ,[32] we decided to generate various FE simulations by varying the preferred mean fiber orientations defined by $\beta_d$, $\beta_m$, and $\beta_p$. Ideally, one should employ inverse FE methods to select the parameter space that matches the experimentally measured displacement field of the rat vagina and, subsequently, create the snapshots in such space for the ROM. Nevertheless, our findings still show the potential of G-ROM and DD-VMS-ROM to provide much faster descriptions of the rat vaginal deformation.

We constructed our G-ROM and DD-VMS ROM using as snapshots the solutions of FE simulations that were obtained for different parameter values (i.e., $p_i$, $\beta_p$, $\beta_m$, and $\beta_d$) (Figures 4 and 5). Since we used commercial software, the last iterations of the Newton–Raphson method that provided the final solutions were selected to generate such snapshots. However, other methods such as the discrete empirical interpolation method and its variants[30] can be employed to generate ROM directly from the nonlinear system of equations that characterize the mechanical behavior of soft tissues. Though we acknowledge that the construction of the snapshots represents a limitation of our study, we believe that our implementation of G-ROM and DD-VMS ROM starting from data obtained from commercial FE software package may allow more users, regardless of their level of expertise in nonlinear FE, to adopt ROM methods.

Both the G-ROM and the DD-VMS-ROM were constructed using ROM bases of dimension $l = 1, ..., 100$. The choice to have $l = 100$ be the maximum dimension of the ROM basis was made using the results for eigenvalue decay reported in Figure 6. In particular, at $l = 100$ we observed a substantial decrease in the eigenvalues, with values below $O(10^{-11})$. From this behavior, we were able to infer that the exhaustion of viable POD basis functions occurred somewhere in the range of $l = 65, ..., 100$. This was confirmed a posteriori by the relative Frobenius norm error results (Figure 8). While this method of choosing a maximum $l$ by observing eigenvalue decay and confirming exhaustion of modes via ROM error results is effective, ideally one should be able select the viable number of modes without such computations. Having this knowledge would minimize the computational time spent on discarding non-viable modes, especially at higher values of $l$ for which the offline computational cost of constructing ROMs is high. One alternative approach for choosing the maximum $l$ is to measure the RIC index defined in Equation (9) as $l$ increased. Following this approach, one usually sets a tolerance close to 1 (e.g., .9999) and considers the maximum $l$ for which the RIC index exceeds this tolerance. However, choosing an appropriate RIC tolerance is not trivial. In our case, when we attempted to follow this approach, the RIC index exceeded a tolerance of .9999 at $l = 5$. Since our viable basis functions were not considered exhausted until $l > 70$ and the relative Frobenius norm error of our ROMs improved by 6 orders of magnitude between $l = 5$ and the threshold of exhaustion, we concluded that the quality of our ROM approximations was dependent on the lower energy POD modes. We could have set the tolerance closer to 1 to achieve results consistent with the eigenvalue decay method, but that would have been just as arbitrary as making an inference based on eigenvalue decay. Thus, in cases like ours, the RIC index method for the selection of the maximum $l$ may not be preferable over the eigenvalue decay method.

In this study, we elected to apply our ROMs solely to reproduce our training data with reasonable accuracy at reduced computational cost. We acknowledge, however, that ROMs can be used to make predictions, using the subspace spanned by ROM basis functions to interpolate or extrapolate the behavior of a FOM that is not included in the training data. For example, Niroomandi et al.[23] used both Grassman manifold fitting and POD with FE piecewise linear interpolation to precompute ROM bases for a set of "most probable" load states and interpolate to new load states using the nearest precomputed states. Pfaller et al.[20] similarly employed the subspace interpolation via Grassmann manifolds and direct basis interpolation, but also considered weighted concatenation methods for both the POD bases and snapshots at different parameters. Additionally, they applied these subspace interpolation methods to gradient-based inverse analysis, using parametric ROMs as a less computationally expensive alternative to the inverse FE method. Given that our current FOM essentially produces load state snapshot matrices for 8 different parameter sets, subspace interpolation

and the parametric ROM inverse analysis methods could certainly be applied. As our work advances, we intend to implement these and similar methods to develop predictive ROMs of vaginal tissue.

Our long-term goal is to develop real-time computational tools that can be used to predict the large deformations of the human vagina in pregnant women. Clearly, the results presented here, both for the FE and ROM, are only capturing the deformations of the rat vagina in simplified ex-vivo settings and, for this reason, their relevance to in-vivo human vagina remains questionable. Evaluating the mechanical properties of the human vaginal tissue in vivo is unethical, especially during pregnancy, since it poses health risks to both the mothers and their babies. For this reason, new computational models, with advanced algorithms, must be developed to assess the deformations of this reproductive organ in real-time by accounting for the differences in material properties, boundary conditions, and geometries of the organ between humans and rodents (or other species).

# 6 | CONCLUSIONS

This computational work leveraged experimental data to develop and validate a FE model of rat vaginal tissue under inflation and leveraged ROM techniques to approximate the results of FE simulations. Specifically, we used the commercial software, *Abaqus*, to construct the FE model and collect snapshots from the FE simulations across eight different collagen fiber distributions, each at 30 load conditions. With these data, we implemented two projection-based ROMs, the standard G-ROM and the DD-VMS-ROM, showing that the DD-VMS-ROM can improve accuracy with a DD correction term for discarded modes. Using these ROMs, we produced approximations of our FE snapshots at a significantly reduced computational cost. To our knowledge, we are the first to implement the DD-VMS-ROM to approximate the mechanical behavior of anisotropic nonlinear elastic soft biological tissues.

We compared the performance of the approximations produced by each ROM in terms of their accuracy and time-savings relative to the FOM. We observed substantial time-savings with both ROM approaches with online simulations that were $O(10^6)$ times faster than the FOM for both G-ROM and DD-VMS-ROM for ROM bases up to dimension $l = 50$. The ROMs would reduce in speed gradually with increasing ROM basis dimension to $O(10^5)$ at $l > 80$ for the G-ROM and $l > 50$ for the DD-VMS-ROM. While both approaches achieved approximations with Frobenius norm error $O(10^{-6})$ relative to the FOM with $l > 70$, within the range $l = 20, ..., 40$, the DD-VMS-ROM outperformed the G-ROM in terms of error by an order magnitude with G-ROM errors ranging from $O(10^{-2})$ to $O(10^{-3})$ compared to the DD-VMS-ROM errors, which ranged from $O(10^{-3})$ to $O(10^{-4})$. Over the same range of ROM basis dimensions, the two approaches were comparable in terms of speed (both $O(10^6)$ times faster than the FOM), indicating a valuable use-case for the DD-VMS-ROM.

Our findings suggest that the ROM approaches employed here are capable of achieving exceptional accuracy when modeling vaginal tissue with nonlinear material properties. Given the success of this proof-of-concept, in future work we plan to investigate the potential for these techniques to approximate models of the vagina with more complex geometries and realistic boundary conditions that better reflect the in vivo conditions of the organ. In addition, we found that the DD-VMS-ROM can approximate the FOM with superior accuracy to the standard G-ROM while achieving a comparable reduction in computational cost. These results are promising for the application of ROMs to computational tools for real-time simulation of childbirth, which would aid obstetricians in recommending a preferred mode of delivery.

## AUTHOR CONTRIBUTIONS
**William Snyder:** data curation (lead); formal analysis (lead); investigation (equal); methodology (lead); software (lead); validation; visualization (lead); writing – original draft (equal); writing – review and editing (lead). **Jeffrey A. McGuire:** formal analysis (supporting); investigation (equal); methodology (supporting); software (supporting); writing – original draft (equal). **Changhong Mou:** formal analysis (supporting); investigation (equal); methodology (supporting); software (supporting); writing – original draft (equal). **David D. Dillard:** funding acquisition (equal); investigation (equal); writing – review and editing (supporting). **Traian Iliescu:** conceptualization (equal); funding acquisition (equal); investigation (equal); methodology (supporting); project administration (supporting); supervision (equal); writing – original draft preparation (equal); writing – review and editing (supporting). **Raffaella De Vita:** conceptualization (equal); funding acquisition (equal); investigation (equal); methodology (supporting); project administration (lead); resources (lead); supervision (equal); visualization (supporting); writing – original draft preparation (equal); writing – review and editing (supporting).

## CONFLICT OF INTEREST
The authors declare no potential conflict of interests.

## DATA AVAILABILITY STATEMENT
The data that support the findings of this study are available from the corresponding author upon reasonable request.

## REFERENCES

1. Betran AP, Ye J, Moller A, Souza JP, Zhang J. Trends and projections of caesarean section rates: global and regional estimates. *BMJ Glob Health*. 2021;6(6):e005671.
2. Martin JA, Hamilton BE, Osterman MJK, Driscoll AK. Births: final data for 2019. *Natl Vital Stat Rep*. 2021;70(2):1-51.
3. Villar J, Valladares E, Wojdyla D, et al. Caesarean delivery rates and pregnancy outcomes: the 2005 who global survey on maternal and perinatal health in Latin America. *Lancet*. 2006;367(9525):1819-1829.
4. Chen S, Grimm MJ. Childbirth computational models: characteristics and applications. *J Biomech Eng*. 2021;143(5):050801.
5. Jing D, Ashton-Miller JA, DeLancey JOL. A subject-specific anisotropic visco-hyperelastic finite element model of female pelvic floor stress and strain during the second stage of labor. *J Biomech*. 2012;45(3):455-460.
6. Luo J, Chen L, Fenner DE, Ashton-Miller JA, DeLancey JOL. A multi-compartment 3-D finite element model of rectocele and its interaction with cystocele. *J Biomech*. 2015;48(9):1580-1586.
7. Gordon MT, DeLancey JOL, Renfroe A, Battles A, Chen L. Development of anatomically based customizable three-dimensional finite-element model of pelvic floor support system: POP-SIM1. 0. *Interface Focus*. 2019;9(4):20190022.
8. Holmes P, Lumley JL, Berkooz G. *Turbulence, Coherent Structures*. Dynamical Systems and Symmetry; 1996.
9. Volkwein S. *Proper Orthogonal Decomposition: Theory and Reduced-Order Modelling. Lecture Notes*. University of Konstanz; 2013 http://www.math.uni-konstanz.de/numerik/personen/volkwein/teaching/POD-Book.pdf
10. Hesthaven JS, Rozza G, Stamm B. *Certified Reduced Basis Methods for Parametrized Partial Differential Equations*. Springer; 2015.
11. Quarteroni A, Manzoni A, Negri F. *Reduced Basis Methods for Partial Differential Equations: an Introduction*. Vol 92. Springer; 2015.
12. Chinesta F, Ladeveze P, Cueto E. A short review on model order reduction based on proper generalized decomposition. *Arch Comput Methods Eng*. 2011;18(4):395-404.
13. Perotto S, Ern A, Veneziani A. Hierarchical local model reduction for elliptic problems: a domain decomposition approach. *Multiscale Model Simul*. 2010;8(4):1102-1127.
14. Gentili GG, Khosronejad M, Bernasconi G, Perotto S, Micheletti S. Efficient modeling of multimode guided acoustic wave propagation in deformed pipelines by hierarchical model reduction. *Appl Numer Math*. 2022;173:329-344.
15. Barrault M, Maday Y, Nguyen NC, Patera AT. An 'empirical interpolation' method: application to efficient reduced-basis discretization of partial differential equations. *C R Acad Sci Paris, Ser*. 2004;I(339):667-672.
16. Chaturantabut S, Sorensen DC. Nonlinear model reduction via discrete empirical interpolation. *SIAM J Sci Comput*. 2010;32(5):2737-2764.
17. Chapelle D, Gariah A, Moireau P, Sainte-Marie J. A galerkin strategy with proper orthogonal decomposition for parameter-dependent problems-analysis, assessments and applications to parameter estimation. *ESAIM: Math Model Numer Anal-Modél Math Anal Numér*. 2013;47(6):1821-1843.
18. Bonomi D, Manzoni A, Quarteroni A. A matrix discrete empirical interpolation method for the efficient model reduction of parametrized nonlinear pdes: application to nonlinear elasticity problems. MATHICSE, Ecole Polytechn. Fédérale de Lausanne, Lausanne, Switzerland, Tech. Rep, 14; 2016.
19. Bonomi D, Manzoni A, Quarteroni A. A matrix deim technique for model reduction of nonlinear parametrized problems in cardiac mechanics. *Comput Methods Appl Mech Eng*. 2017;324:300-326.
20. Pfaller MR, Cruz Varona M, Lang J, Bertoglio C, Wall WA. Using parametric model order reduction for inverse analysis of large nonlinear cardiac simulations. *Int J Numer Method Biomed Eng*. 2020;36(4):e3320.
21. Barone A, Carlino MG, Gizzi A, Perotto S, Veneziani A. Efficient estimation of cardiac conductivities: a proper generalized decomposition approach. *J Comput Phys*. 2020;423:109810.
22. Dogan F, Celebi MS. Real-time deformation simulation of non-linear viscoelastic soft tissues. *Simulation*. 2011;87(3):179-187.
23. Niroomandi S, Alfaro I, Cueto E, Chinesta F. Accounting for large deformations in real-time simulations of soft tissues based on reduced-order models. *Comput Methods Programs Biomed*. 2012;105(1):1-12.
24. Niroomandi S, González D, Alfaro I, et al. Real-time simulation of biological soft tissues: a pgd approach. *Int J Numer Method Biomed Eng*. 2013;29(5):586-600.
25. Cueto E, Chinesta F. Real time simulation for computational surgery: a review. *Adv Model Simul Eng Sci*. 2014;1(1):1-18.
26. Niroomandi S, Alfaro I, Cueto E, Chinesta F. Real-time deformable models of non-linear tissues by model reduction techniques. *Comput Methods Programs Biomed*. 2008;91(3):223-231.

27. Niroomandi S, Alfaro I, Gonzalez D, Cueto E, Chinesta F. Real-time simulation of surgery by reduced-order modeling and x-fem techniques. *Int J Numer Method Biomed Eng*. 2012;28(5):574-588.

28. Radermacher A, Reese S. Proper orthogonal decomposition-based model reduction for non-linear biomechanical analysis. *Int J Mater Eng Innov*. 2013;4(2):149-165.

29. Radermacher A, Reese S. A comparison of projection-based model reduction concepts in the context of nonlinear biomechanics. *Arch Appl Mech*. 2013;83(8):1193-1213.

30. Radermacher A, Reese S. Pod-based model reduction with empirical interpolation applied to nonlinear elasticity. *Int J Numer Methods Eng*. 2016;107(6):477-495.

31. McGuire JA, Crandall CL, Abramowitch SD, De Vita R. Inflation and rupture of vaginal tissue. *Interface Focus*. 2019;9(4):20190029.

32. McGuire JA, Monclova JL, Coariti ACS, et al. Tear propagation in vaginal tissue under inflation. *Acta Biomater*. 2021;127:193-204.

33. Gasser TC, Ogden RW, Holzapfel GA. Hyperelastic modelling of arterial layers with distributed collagen fibre orientations. *J R Soc Interface*. 2006;3(6):15-35.

34. Simo JC, Taylor RL. Quasi-incompressible finite elasticity in principal stretches. Continuum basis and numerical algorithms. *Comput Methods Appl Mech Eng*. 1991;85(3):273-310.

35. Kim N-H. *Introduction to Nonlinear Finite Element Analysis*. Springer Science & Business Media; 2014.

36. Sirovich L. Turbulence and the dynamics of coherent structures. I. Coherent structures. *Q Appl Math*. 1987;45(3):561-571.

37. Ahmed SE, Pawar S, San O, Rasheed A, Iliescu T, Noack BR. On closures for reduced order models — a spectrum of first-principle to machine-learned avenues. *Phys Fluids*. 2021;33(9):091301.

38. Hughes TJR, Feijóo GR, Mazzei L, Quincy J-B. The variational multiscale method – a paradigm for computational mechanics. *Comput Methods Appl Mech Eng*. 1998;166(1):3-24.

39. Liu J, Marsden AL. A unified continuum and variational multiscale formulation for fluids, solids, and fluid–structure interaction. *Comput Methods Appl Mech Eng*. 2018;337:549-597.

40. Mou C, Koc B, San O, Rebholz LG, Iliescu T. Data-driven variational multiscale reduced order models. *Comput Methods Appl Mech Eng*. 2021;373:113470.

41. Xie X, Mohebujjaman M, Rebholz LG, Iliescu T. Data-driven filtered reduced order modeling of fluid flows. *SIAM J Sci Comput*. 2018;40(3):B834-B857.

42. Mou C, Liu H, Wells DR, Iliescu T. Data-driven correction reduced order models for the quasi-geostrophic equations: a numerical investigation. *Int J Comput Fluid Dyn*. 2020;34:147-159.

43. Brunton SL, Kutz JN. *Data-Driven Science and Engineering: Machine Learning, Dynamical Systems, and Control*. Cambridge University Press; 2019.

44. Huntington AJ, Udayasuryan B, Du P, Verbridge SS, Abramowitch SD, De Vita R. Smooth muscle organization and nerves in the rat vagina: a first look using tissue clearing and immunolabeling. *Ann Biomed Eng*. 2022;50:440-451.

45. Tan T, De Vita R. A structural constitutive model for smooth muscle contraction in biological tissues. *Int J Non-Linear Mech*. 2015;75:46-53.

46. Pandolfi A, Vasta M. Fiber distributed hyperelastic modeling of biological tissues. *Mech Mater*. 2012;44:151-162.

47. Gizzi A, Pandolfi A, Vasta M. A generalized statistical approach for modeling fiber-reinforced materials. *J Eng Math*. 2018;109:211-226.

48. Huntington A, Rizzuto E, Abramowitch S, Del Prete Z, De Vita R. Anisotropy of the passive and active rat vagina under biaxial loading. *Ann Biomed Eng*. 2019;47(1):272-281.

49. Huntington A, Donaldson K, De Vita R. Contractile properties of vaginal tissue. *J Biomech Eng*. 2020;142(8):1-9.

50. Huntington A, Abramowitch SD, Moalli PA, De Vita R. Strains induced in the vagina by smooth muscle contractions. *Acta Biomater*. 2021;129:178-187.